THE JOURNAL OF PHYSICAL CHEMISTRY C

Article

Cite This: J. Phys. Chem. C 2019, 123, 19602−19609

pubs.acs.org/JPCC

Crystallographic Orientation and Surface Charge-Tailored Continuous Polarization Rotation State in Epitaxially Ferroelectric Nanostructures

Yanpeng Feng,[†,‡] Heng Zhang,[†,§] Yinlian Zhu,*[,†] Yujia Wang,[†] Yunlong Tang,[†] Minjie Zou,[†,§] Mengjiao Han,[†,‡] Wanrong Geng,[†,§] Jinyuan Ma,[†,§,∥] and Xiuliang Ma*[,†,∥]

[†]Shenyang National Laboratory for Materials Science, Institute of Metal Research, Chinese Academy of Sciences, Wenhua Road 72, 110016 Shenyang, China

[‡]Center of Materials Science and Optoelectronics Engineering, University of Chinese Academy of Sciences, Yuquan Road 19, 100049 Beijing, China

[§]School of Material Science and Engineering, University of Science and Technology of China, Hefei 230026, China

[∥]State Key Lab of Advanced Processing and Recycling on Non-ferrous Metals, Lanzhou University of Technology, Langongping Road 287, 730050 Lanzhou, China

Supporting Information

ABSTRACT: The multiple polarization states driven by polarization rotation could trigger giant piezoelectric responses in electromechanical sensors. Theoretically and experimentally, polarization rotation in ferroelectrics was contentiously reported in $PbTiO_3$ thin films, which may result from low symmetric phases, flexoelectricity, or interfacial oxygen octahedral coupling. In this work, 5 nm $PbTiO_3$ was grown on $SrRuO_3$-buffered (001)- and (101)-oriented $SrTiO_3$ substrates. By using piezoresponse force microscopy and (scanning) transmission electron microscopy, self-assembled $PbTiO_3$ nanostructures with a triangular-prism-shaped morphology (average width about 30 nm) were observed on the (101)-oriented $SrTiO_3$ substrate. Particularly, continuous polarization rotation state was confirmed in each $PbTiO_3$ nanostructure, where the rotation angle is up to 90° approximately from the left side to the right side. In collaboration with phase-field simulations, it is proposed that the surface positive charge accumulation facilitates the formation of continuous polarization rotation. Piezoresponse force microscopy measurements indicate that these [101]$PbTiO_3$ nanostructures with polarization rotation display a superior piezoelectric response compared with the [001]$PbTiO_3$ thin film. These results not only shed light on understanding the polarization rotation mechanism in ferroelectrics but also are expected to provide useful information for developing the high performance of electromechanical devices.

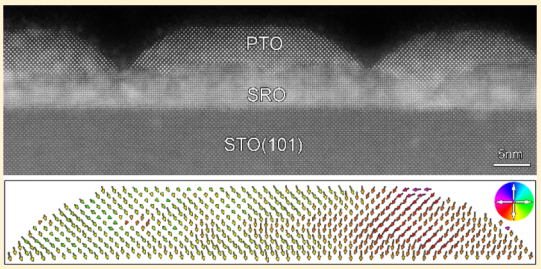

1. INTRODUCTION

Ferroelectrics exhibiting switchable spontaneous polarization under applied electric field have many potential applications in nonvolatile ferroelectric random access memories, actuators, and transducers that require sizes down to a nanometer range.[1,2] The multiple polarization states in ferroelectric thin films and nanostructures have attracted much attention since they may generate novel exotic physical phenomena which have potential applications in future electronics. For instance, recently, flux-closure arrays,[3] polar vortices,[4] dipole waves, and dipole disclinations[5] have been successively observed in $PbTiO_3/SrTiO_3$ multilayer films and superlattices. These peculiar topological configurations suggest new manipulations of rotations of electric dipoles. Besides, the exotic polarization rotation patterns induced by defects were observed in multiferroic $BiFeO_3$ thin films.[6] Generally, the multiple polarization states tailored by polarization rotation are accompanied by the giant piezoelectric responses, which can be used to develop high-performance of electromechanical sensors.[7−9] Thus, it is important to explore the polarization rotation mechanism in ferroelectric thin films.

In the past decades, the phenomena and mechanisms of polarization rotation in ferroelectric crystals and thin films were widely reported and thoroughly discussed. For instance, it is reported that a morphotropic phase boundary region can exist when pure $PbTiO_3$ (PTO) powder is under the condition of high pressure at low temperature, and consequently the polarization rotation forms more easily between different symmetries (tetragonal, monoclinic, and rhombohedral), which gives rise to a large electromechanical coupling.[8] Moreover, the polarization rotates away from the tetragonal axis and a low-symmetry phase arises in a fully epitaxial PTO

Received: May 16, 2019
Revised: July 8, 2019
Published: July 22, 2019

DOI: 10.1021/acs.jpcc.9b04654
J. Phys. Chem. C 2019, 123, 19602−19609

thin film of 5 nm thickness under the tensile strain.[10] Furthermore, a previous study indicated that the flexoelectric effect, which is the coupling between polarization and strain gradient, can force spontaneous polarization of 30 nm thick PTO films to rotate away from the normal.[11] Recently, polarization rotation tailored by interfacial oxygen octahedral coupling in ultrathin PTO films under negligible strains has been observed by aberration-corrected scanning transmission electron microscopy (TEM) and simultaneously demonstrated by first-principle calculations.[12] So far, most studies on polarization rotation have focused on (001)-oriented films. However, recent studies have revealed that the crystallographic orientation of ferroelectric films has a great effect on the domain configuration,[13,14] dielectric property,[15] and ferroelectric switching behavior.[16] Furthermore, theoretically, the temperature-strain phase diagrams of single domain (101)-oriented PTO thin films indicated that the PTO films grown on $SrTiO_3$ (STO) substrates could be a monoclinic a_2c phase or an orthorhombic c phase, which means that the polarization rotation may exist in PTO/STO(101) films due to the monoclinic−orthorhombic ferroelectric morphotropic phase boundary.[17]

In this work, we deposited 5 nm $PbTiO_3$ films on (001)- and (101)-oriented $SrRuO_3$ (SRO)-buffered STO substrates by pulsed laser deposition (PLD). By using TEM, including the diffraction contrast analysis and aberration-corrected high-angle annular dark field (HAADF) scanning TEM (STEM), a triangular-prism-shaped morphology with the average width of about 30 nm was observed in the PTO films grown on the (101)-oriented SRO-buffered STO substrates, forming the stripe PTO nanostructures. Atomically resolved HAADF-STEM imaging indicates that continuous polarization rotation arises in the [101]PTO nanostructure and the rotation angle is up to 90° approximately from the left to right side in a PTO nanostructure, whereas uniform polarization with direction along the *c* axis of PTO appear in the [001]PTO thin films. Phase-field simulations demonstrate that the surface charge accumulation of [101]PTO nanostructures has a great effect on the formation of continuous polarization rotation. Piezoresponse force microscopy (PFM) reveals that [101]PTO nanostructures have a superior piezoelectric response compared with [001]PTO thin films.

2. METHODS

2.1. Film Deposition. The PTO films were epitaxially fabricated on SRO-buffered (001)- and (101)-oriented STO substrates by PLD with a Coherent ComPexPRO KrF (λ = 248 nm) excimer laser. The target−substrate distance was 80 mm. The buffer layer of SRO thin films were deposited on the STO(001) and STO(101) substrates at the substrate temperature of 700 °C, with a laser energy density of 1.5 J/cm^2, a repetition rate of 4 Hz, and under the oxygen partial pressure of 50 mTorr. Before the deposition of the SRO thin film, the substrate was heated to 800 °C for 10 min to clean the substrate surface and then cooled down to 700 °C for film deposition. For deposition of the PTO layer, the substrate temperature of 700 °C, an oxygen partial pressure of 75 mTorr, a laser energy density of 2 J/cm^2, and a repetition rate of 4 Hz were employed. The stoichiometric SRO ceramic target was used for deposition of the SRO layer, whereas the 3% Pb-enriched ceramic target was used for deposition of the PTO layer. After deposition, the films were maintained at 700 °C for 5 min in an oxygen pressure of 200 Torr and then cooled down to room temperature with the cooling rate of 5 °C/min.

2.2. Topography and PFM Measurements. Surface topography and PFM measurements were performed by using a scanning probe microscope (Cypher, Asylum Research) at room temperature. The nonconductive silicon cantilever (AC240TS-R3, Asylum Research) was used for surface topography measurement. The tip radius was about 7 nm, and the force constant was about 2 N/m. The conductive silicon cantilever with Pt/Ir coating (ARROW-EFM-50, NanoWorld) was used for local PFM hysteresis loop measurements. This cantilever has the length of 240 μm, the width of 35 μm, the resonance frequency of 75 kHz, and the force constant of 2.8 N/m. Before measuring the local PFM hysteresis loop, the cantilever was calibrated by using Sader and thermal noise methods[18,19] carried out by Asylum software (Asylum Research). During testing, a sequence of dc voltage with the maximum value of 10 V was applied to trigger ferroelectric switching and a modulated ac voltage of 2 V was used to detect the amplitude and phase of surface fluctuation.

2.3. TEM Sample Preparation, (S)TEM Imaging, Strain Analysis, and Determination of the Positions of Atoms. Cross-sectional TEM samples were prepared by conventional slicing, gluing, grinding, dimpling, and ion milling. A PIPS 691 (Gatan) was used for final ion milling. Plane-view TEM samples were grinded, dimpled, and ion milled only from the substrate side. The final voltage of milling was less than 0.5 kV to reduce ion beam damage. Two-beam dark-field images were acquired by Tecnai G^2 F30 transmission electron microscope (TEM). All HAADF-STEM images were acquired by an aberration-corrected scanning transmission electron microscope (FEI, Titan Cubed 60−300 kV microscope) equipped with double aberration (C_s) correctors from CEOS, a high-brightness field-emission gun, and a monochromator operating at 300 kV. The beam convergence angle was 25 mrad during STEM observation. Strain fields were extracted by using geometry phase analysis (GPA), carried out by Gatan Digital Micrograph software. The positions of atom columns in high-resolution HAADF-STEM images were determined by two-dimensional (2D) Gaussian peak fittings, which was based on the Matlab software.

2.4. Phase Field Simulation. A three-dimensional (3D) phase-field model was constructed to simulate the polarization distribution in the [101]PTO nanostructures. The primary order parameter was chosen as the polarization vector $\boldsymbol{P} = (P_1, P_2, P_3)$. The evolution of polarization in PTO nanostructures was described by the time-dependent Ginzburg−Landau equation: $\partial P_i/\partial t = -L\cdot\delta F/\delta P_i$, where F is the system total free-energy density including the Landau bulk energy density, gradient energy density, elastic energy density, and electrostatic energy density. The PTO nanostructure was simulated as a trapezoidal prism, which is covered by positive surface charges. The model dimension of the trapezoidal prism is a mesh of 64 × 32 × 25 discrete grid points and the grid spacing is $x_0 = y_0$ = 1 nm and z_0 = 0.2 nm in our simulation. As a result, the real size of the trapezoidal prism is 64 × 32 × 5 nm^3. The periodic boundary condition was applied along the x and y directions. In the experiment, the nanostructures are grown on the SRO electrode and surrounded by vacuum. Hence, we applied the short- and open-circuit electric boundary conditions on the bottom and top of the nanostructure, respectively. The elastic boundary condition was chosen to be traction free on top of the nanostructure and zero displacement on the bottom of the

DOI: 10.1021/acs.jpcc.9b04654
J. Phys. Chem. C 2019, 123, 19602−19609

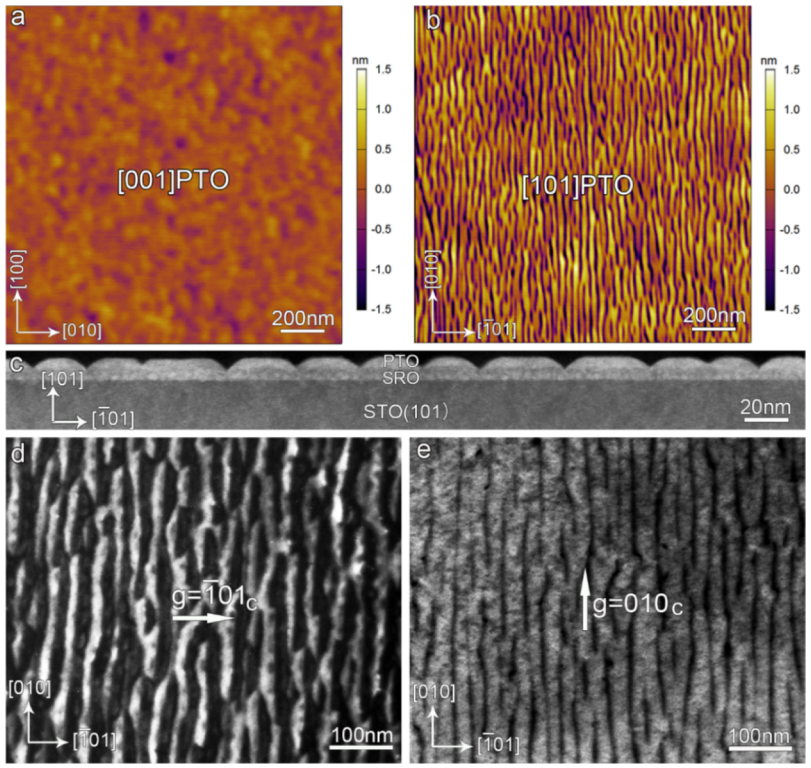

Figure 1. (a) Surface topographic image of [001]PTO thin films showing a smooth surface. (b) Surface topographic image of [101]PTO films indicating that the stripe nanostructures appear. (c) Cross-sectional HAADF-STEM image of [101]PTO films viewed along in-plane [010] direction. Note the regular PTO nanostructure arrays with trapezoidal shape. Plane-view two-beam dark-field TEM images of [101]PTO films obtained near the [101] zone axis of STO taken with diffraction vectors of (d) $\mathbf{g} = \bar{1}01_c$ and (e) $\mathbf{g} = 010_c$.

simulation region. All of the material parameters employed in the simulations are adopted from previous literature.[20] More simulation details can be found in the Supporting Information.

3. RESULTS & DISCUSSION

At room temperature, PTO is a typical tetragonal ferroelectrics with lattice parameters of $a = b = 3.899$ Å and $c = 4.153$ Å,[21] whereas STO exhibits a cubic structure with lattice parameters of $a = b = c = 3.905$ Å. In contrast to the (001) orientation, STO(101) substrates have two different in-plane crystal axes, [010] and [$\bar{1}$01], which bring asymmetric biaxial strain for PTO thin films.[13,22] The surface topographies of [001]PTO and [101]PTO thin films are shown in Figure 1a,b, respectively. From Figure 1a, it is seen that the [001]PTO thin film exhibits a very smooth surface with the surface root-mean-square (rms) roughness of 152 pm. However, from Figure 1b, it is noted that the [101]PTO features a stripe surface morphology with the surface RMS of 520 pm, indicating the formation of the stripe nanostructures in the [101]PTO film. All stripes are almost along the in-plane [010] direction of the STO substrate, and the average width of these stripes is about 30 nm.

Advanced TEM techniques, including diffraction contrast analysis and atomically resolved HAADF-STEM imaging, were used to further investigate the details of the [001]PTO thin films and [101]PTO nanostructures. For [001]PTO thin films, the cross-sectional high-resolution HAADF-STEM imaging taken along the in-plane [100] direction is shown in Figure S1a, indicating that both the PTO/SRO and SRO/STO interfaces are very sharp. It is also seen that the surface of PTO is smooth, which is consistent with the atomic force microscope topography. A cross-sectional low-magnification HAADF-STEM image of [101]PTO taken along the in-plane [010] direction of STO is shown in Figure 1c. A trapezoidal-shaped morphology is easily seen in [101]PTO nanostructures. Figure 1d,e are plane-view two-beam dark-field TEM images of the [101]PTO nanostructures taken by different reflections of $\mathbf{g} = \bar{1}01_c$ and $\mathbf{g} = 010_c$, respectively, where the subscript "c" denotes cubic STO substrate. Figure 1d, taken with the reflection of $\mathbf{g} = \bar{1}01_c$, shows the PTO stripe nanostructure arrays with a regular arrangement. For each stripe nanostructure, it is noted that the nanostructure displays bright contrast on the left side, while it displays dark contrast on the right side. Thus, strain modulations may be expected along the [$\bar{1}$01] direction in each PTO nanostructure here, such as continuous lattice rotation, which may be related to continuous polarization rotation in PTO nanostructures. However, it displays a uniform contrast in each nanostructure when taken with the reflection of $\mathbf{g} = 010_c$ under two-beam dark-field conditions, which may indicate that the in-plane strain is uniform along the [010] direction in a PTO nanostructure.

To further display the details of [101]PTO nanostructures, atomic-resolved HAADF-STEM images were acquired by aberration-corrected STEM. Figure 2a is a high-resolution HAADF-STEM image of [101]PTO nanostructures acquired along the in-plane [010] direction of STO. It is seen that the thicknesses of the PTO layer and the SRO buffered layer are about 5 and 6 nm, respectively. The interface between PTO and SRO layers is somewhat fluctuated. For a nanostructure, the trapezoidal-like shape can be found with the upper surface of (101) plane of PTO and the two side surfaces of (100) and (001) planes of PTO, respectively. The inset is the fast Fourier

DOI: 10.1021/acs.jpcc.9b04654
J. Phys. Chem. C 2019, 123, 19602−19609

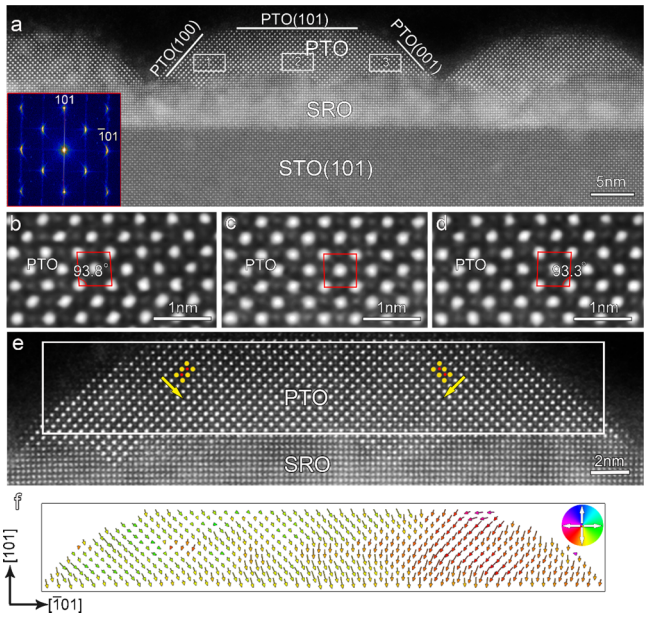

Figure 2. HAADF-STEM images of PTO/SRO/STO(101) nanostructures taken along the [010] direction. (a) Atomically resolved HAADF-STEM image showing the upper surface of nanostructures is (101) of PTO, whereas the two sides surface are {100} of PTO. The inset is the FFT image of (a) showing the reciprocal space information. The obvious feature of the in-plane ($\bar{1}$01) spot is the highly dispersive distribution, whereas the out-of-plane (101) spot is almost not elongated. Three rectangles labeled as "1−3" are three typical areas magnified in (b−d). Note the lattice distortion of (b,d) compared with (c), which indicates a large shear strain in PTO nanostructures along the in-plane [$\bar{1}$01] direction. (e) Atomic-resolution HAADF-STEM image of the PTO nanostructure. The yellow arrows denote the directions of spontaneous polarization (P_s), which are opposite to the directions of displacement of Ti atomic columns. The yellow and red circles in (e) denote the positions of Pb and Ti columns, respectively. (f) Mapping of reversed δ_{Ti} vectors corresponding to the white rectangular box in Figure 2e. The arrows with different colors denote the different directions of spontaneous polarizations in a PTO nanostructure.

transformation (FFT) image of Figure 2a, showing the reciprocal space information in [101]PTO nanostructures. It is noted that the out-of-plane (101) spot is very sharp and almost not elongated, whereas the in-plane ($\bar{1}$01) spot exhibits the highly dispersive and cambered distribution. Three typical areas in a nanostructure labeled as "1−3" in Figure 2a are magnified and shown in Figure 2b−d, respectively. It is found that the left PTO lattices are tilted to the left, the right PTO lattices are tilted to the right, and the middle PTO lattices keep almost unchanged. The tilting angles of the two side lattices relative to the middle lattice in a PTO nanostructure are about 3.5°. Figure 2e is an atomic-scale HAADF-STEM image of the [101]PTO nanostructure, which was taken along the [010] direction. The yellow and red circles denote the position of Pb and Ti atom columns, respectively (Pb atom columns are bright, whereas Ti atom columns are weak, which is based on the HAADF-STEM imaging due to their atomic numbers: heavy Pb (82) and light Ti (22) atoms[3−5,23]). The two yellow arrows denote the P_S directions of the [101]PTO nanostructure, which are opposite to the displacements of Ti atoms (δ_{Ti}). It is easily seen that the polarization directions of PTO unit cells point to the lower right corner on the left side, but lower left corner on the right side. Figure 2f displays the 2D mapping of reversed δ_{Ti} vectors corresponding to the white rectangular box in Figure 2e. The arrows with different colors denote the different directions of spontaneous polarizations (P_S). It is clearly seen that the polarization directions gradually rotate from the left side to the right side of the [101]PTO nanostructure, where the polarization rotation angle is almost up to 90°. Besides, no obvious domain walls appear in the [101]PTO nanostructures. In contrast, all polarization directions of PTO unit cells are almost along [00$\bar{1}$] of PTO and point to the PTO/SRO interface in the [001]PTO thin film, as shown in Figure S1c, which indicates that no obvious polarization rotation appears in the [001]PTO thin film.

The strain distribution in [101]PTO nanostructures was analyzed by performing GPA, which is an effective tool to display long-range strain information.[24] Figure 3a,b are in-plane strain (ε_{xx}) and shear strain (ε_{xy}) maps corresponding to Figure 2a, respectively. The yellow dotted lines denote the

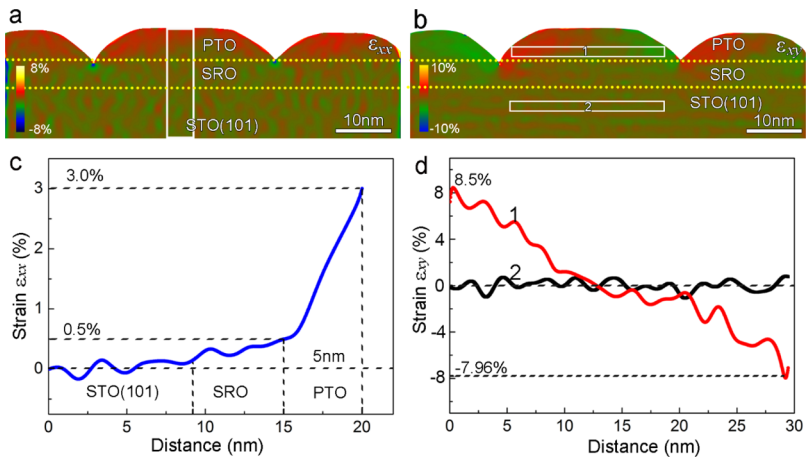

Figure 3. GPA for strain analysis of Figure 2a showing the strain distribution of PTO nanostructures. (a) In-plane strain map (ε_{xx}) and (b) shear−strain map (ε_{xy}). The STO substrate is chosen as the reference. Note the continuous variation of in-plane strain (a) and shear strain (b) in PTO nanostructures along the out-of-plane and in-plane directions, respectively. One line profile labeled in (a) and two line profiles labeled in (b) were visualized in (c,d), respectively, which show continuous increase of ε_{xx} along the out-of-plane direction and continuous decrease of ε_{xy} along the in-plane direction. The linear strain gradient of ε_{xx} and ε_{xy} can be estimated from the curves, which are both in about 10^6/m order.

DOI: 10.1021/acs.jpcc.9b04654
J. Phys. Chem. C 2019, 123, 19602−19609

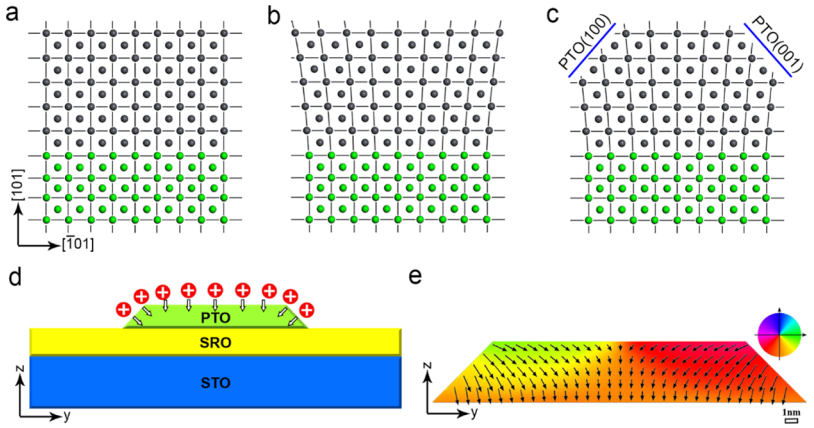

Figure 4. (a–c) Strain release models showing how the PTO nanostructures form (Ti and O atoms are omitted). (a) Full strained film on a lattice-mismatched substrate. (b) Strain relaxation due to substrate clamping causing in-plane lattice expansion. Continuous variation of in-plane strains is formed along the out-of-plane direction. (c) (100) and (001) planes of PTO are introduced to balance the total energy due to their lower surface energies. (d,e) Phase-field simulations of (101)-oriented PTO nanostructures. (d) Schematic diagram of a 5 nm thick PTO nanostructure grown on an STO(101) substrate with an SRO buffered layer. Positive surface charges are accumulated on the surface of $PbTiO_3$ nanostructures due to the accumulation of oxygen vacancies at the surface, which generates the downward electric field. (e) Polarization distribution of the PTO nanostructure obtained from phase-field simulations.

PTO/SRO and SRO/STO(101) interfaces. From Figure 3a, it is seen that there is an obvious difference of in-plane strain between [101]PTO nanostructures and STO(101) substrates. Especially, at the surface of PTO nanostructures, there is an obvious increase for ε_{xx}, which indicates that the PTO nanostructures have in-plane lattice expansion at the surfaces. From Figure 3b, obvious contrast variation appears from the left side to the right side in the PTO nanostructure. One line profile marked by a white rectangular box in Figure 3a is shown in Figure 3c. This line profile shows the in-plane strain variation from the STO(101) substrate to the SRO buffer layer and PTO nanostructures. Note that the strain in the STO(101) substrate is chosen as a reference and set to be zero. Compared with the STO(101) substrate, the in-plane strain in the SRO layer increases a little; whereas in PTO nanostructures, the in-plane strain has a significant increase and the value of ε_{xx} reaches 3%. Importantly, it is noted that there is a linear in-plane strain gradient in PTO nanostructures and the strain gradient of ε_{xx} in PTO is up to 5×10^6 m^{-1}, as estimated by the slope of the curve. Similarly, two line profiles marked as two white rectangular boxes (labeled as "1" and "2", respectively) in Figure 3b are shown in Figure 3d. The shear strain in the STO(101) substrate is also set to zero. Continuous shear strain variation from the left side to the right side in a PTO nanostructure can be seen clearly, which reveals that the PTO lattices take a gradual change in PTO nanostructures. It is also consistent with the diffraction contrast analysis (Figure 1d). Such shear–strain variation results a large linear shear strain gradient ($\sim 5.5 \times 10^6$ m^{-1}), as shown in Figure 3d.

For the [101]PTO thin films grown on STO(101) substrates, the lattice mismatch values between the stress-free thin film and substrate along the [010] and [$\bar{1}$01] directions can be calculated by the following formulas[25]

$$\delta(010) = \frac{a_s - a_f}{a_s} \times 100\% \quad (1)$$

and

$$\delta(\bar{1}01) = \frac{\sqrt{2}\,a_s - \sqrt{({a_f}^2 + {c_f}^2)}}{\sqrt{2}\,a_s} \times 100\% \quad (2)$$

where subscripts "f" and "s" denote the PTO thin film and STO(101) substrate, respectively. Thus, the lattice mismatch values along the [010] and [$\bar{1}$01] directions are determined as 0.15 and −3.15%, respectively, which indicates that the [101]PTO thin film is strained asymmetrically in the two in-plane directions. The asymmetric biaxial strains may induce a transition of coherently strained 2D films to 3D nanostructures.

To interpret the formation of trapezoidal-shaped stripe nanostructures and polarization rotation behavior in the [101]PTO film, the growth mode needs to be paid more attention. We first consider the in-plane asymmetric strain relaxations in the system.[26,27] Figure 4a is a schematic of a coherently strained 2D [101]PTO film. The gray and green circles denote the Pb and Sr atoms, respectively, whereas the Ti and O atoms are omitted. It is seen that if the [101]PTO film is coherently epitaxial on the STO(101) substrate, the PTO film has a full-strained constraint at the (101) plane. However, a large compressive strain (~3.15%) along the in-plane [$\bar{1}$01] direction will be imposed in the [101]PTO film, which can be relaxed laterally along the [$\bar{1}$01] directions. As the upper PTO unit cells are kept away from the substrate and have a smaller clamp effect, compared with the lower PTO unit cells closer to the substrate, the in-plane [$\bar{1}$01] directional strain of PTO is gradually relaxed from lower to upper, which results in the lattice planes gradually expanding along the in-plane [$\bar{1}$01] direction as shown in Figure 4b. Thus, it causes shear strain which arises along the [$\bar{1}$01] direction in PTO. Furthermore, the lattice planes of the upper PTO unit cells have a larger expansion along the in-plane [$\bar{1}$01] direction than the lower PTO unit cells, resulting in the strain gradient along the out-of-plane direction simultaneously. It is pointed out that the mismatch strain along the in-plane [010] direction is so small that the (010) lattice planes of PTO match well with the STO substrate.[26]

Next, the formation of 3D [101]PTO nanostructures with two sides of {100} lattice planes can be understood with the

DOI: 10.1021/acs.jpcc.9b04654
J. Phys. Chem. C 2019, 123, 19602−19609

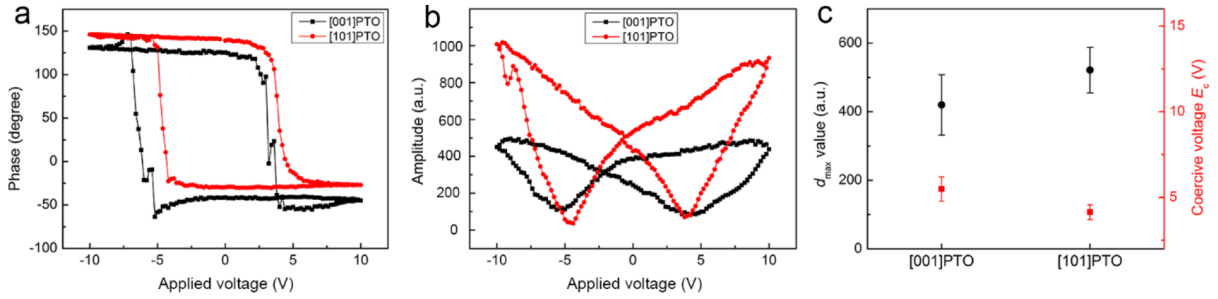

Figure 5. Local PFM hysteresis loop measurements of [001]PTO thin films and [101]PTO nanostructures. (a) Phase hysteresis loops and (b) amplitude hysteresis loops. (c) Statistical results of d_{max} values and coercive voltages of [001]PTO thin films and [101]PTO nanostructures.

surface energy consideration, as shown in Figure 4c. It is reported that the surface energies of {100} planes are much smaller than those of the {101} planes.[28] Although the formation of [101]PTO nanostructures may increase a small amount of surface area, more (100) and (001) planes with lower surface energy are exposed, which cause the reduction of the surface energy from 2D films to 3D nanostructures. Thus, the in-plane strain relaxation and the reduction of surface energy facilitate the transition from a fully strained 2D film to 3D nanostructures, which causes the formation of self-assembled [101]PTO nanostructure arrays in the present study.

Last, the continuous polarization rotation in [101]PTO nanostructures may result from a flexoelectric effect. The giant linear strain gradient exceeds 10^6 m^{-1} (defined as ΔS, $\Delta S = d\varepsilon/dx$) in the present [101]PTO nanostructures, which can induce the flexoelectric polarization (P_f) according to the flexoelectric effect as reported previously.[29] It is known that the flexoelectric coefficient (f) for perovskite ferroelectrics is quite small ($f \approx e/a$, where e is electronic charge and a is the lattice parameter), which is on the order of 10^{-9} to 10^{-8} C/m.[30,31] The induced P_f is about several $\mu C/cm^2$ as calculated by the formula $P_f = f \times \Delta S$. However, the spontaneous polarization (P_s) of bulk PTO is very large ($\approx$84 $\mu C/cm^2$). Furthermore, the value of flexoelectric polarization (P_f) is a constant due to the linear strain gradient. Thus, the flexoelectric polarization can just force the spontaneous polarization of these [101]PTO ferroelectric nanostructures to rotate away from the normal with a small constant angle and cannot be strong enough to cause continuous polarization rotation as we observed experimentally.

Instead of the flexoelectric effect, it is also reported that the surface charge accumulation in ferroelectric $BiFeO_3$ nanoislands can modulate the polarization distribution of the nanoislands.[32,33] When PTO is deposited on the SRO-buffered STO substrates in high vacuum, positively charged oxygen vacancies are inevitably formed on the surface of the PTO layer.[34] Thus, we consider that the formation of exotic polarization rotation in our [101]PTO nanostructures may be ascribed to the surface oxygen vacancy accumulation. The phase-field simulations were used to verify the deduction. We modeled the nanostructure as a trapezoidal prism with its cross-sectional dimension 32 × 5 nm^2, which corresponds to the experimental result (30 × 5 nm^2), as shown in Figure S2. Figure 4d shows the schematic of a 5 nm thick PTO nanostructure grown on an STO(101) substrate with an SRO buffered layer. Positive surface charges of about 1.5 C/m^2 derived from oxygen vacancies are assumed on all surfaces of the [101]PTO nanostructure. Other simulation details can be found in the Supporting Information. The equilibrium polarization distribution of the PTO nanostructure is shown in Figure 4e. Arrows represent the magnitudes and directions of polarization in the $y-z$ plane, and color scales show the angular distribution of polarization. The polarization distribution is axisymmetric. From the left side to the right side in a nanostructure, the polarization rotates continuously, which is consistent with the experimental polarization distribution in Figure 2f. Thus, we can conclude that the accumulation of positive charges on the surface causes the continuous polarization rotation in [101]PTO nanostructures.

To further reveal how the continuous polarization rotation affects the macroscopic ferroelectric and piezoelectric properties of [101]PTO nanostructures, we have performed PFM measurements on the [001]PTO film and [101]PTO nanostructures, where the [001]PTO thin film is used for comparison. The dual ac resonance tracking mode was used to test local PFM hysteresis loops, which can minimize topographic cross-talk and enhance signal-to-noise (S/N) ratio simultaneously.[35] Figure 5a,b show typical phase hysteresis loops and amplitude hysteresis loops of the [001]PTO films and [101]PTO nanostructures, respectively. It is seen that these two phase hysteresis loops have a well-defined square loop feature, indicating the existence of ferroelectric switching behavior in the [001]PTO film and [101]PTO nanostructures.[36,37] Meanwhile, in Figure 5a, the coercive voltages (E_c) can be acquired from phase hysteresis loops, as E_c = 4.9 V for [001]PTO films, whereas E_c = 4.2 V for [101]PTO. In Figure 5b, the amplitude hysteresis loops measured under "off" state display a typical "butterfly shape". The value of the amplitude [max] was acquired, which was divided by applied ac voltage (2 V) to deduce the local piezoelectric coefficient, d_{max} that represents the piezoresponse after applied dc electrical poling.[38,39] To reveal the differences in both piezoresponse and coercive voltage more precisely, the statistical d_{max} and E_c values of [001]PTO films and [101]PTO nanostructures are all shown in Figure 5c. It is found that the [101]PTO nanostructures exhibit a higher d_{max} value and a lower coercive voltage, indicating that the [101]PTO nanostructures manifest a superior piezoelectric response and an easier ferroelectric switching behavior. It is known that the piezoelectric response of ferroelectric thin films depends on two factors.[40] On one hand, phase structures and polarization rotation should affect the intrinsic piezoelectric response of films.[7,8] On the other hand, the extrinsic contributions to the piezoelectric response of films may also appear because of the movement of domain walls away from the equilibrium positions under the external electric field.[40] In this work, the [101]PTO nanostructures exhibit continuous polarization

DOI: 10.1021/acs.jpcc.9b04654
J. Phys. Chem. C 2019, 123, 19602−19609

rotation, which contributes to the intrinsic piezoelectric response. Similar phenomenon of a large piezoelectric response being driven by polarization rotation in $BaTiO_3$, $PbTiO_3$, and $(Ba,Ca)(Zr,Ti)O_3$ have been reported previously.[7,8,41] Besides, it was demonstrated that (001)-oriented discrete $PbZr_{0.2}Ti_{0.8}O_3$ nano-islands can significantly reduce the clamping effects from substrates, thereby promoting the movement of ferroelastic walls, which can strengthen extrinsic contributions to the piezoelectric response and ferroelectric switching.[42] Thus, in this work, the formation of [101]PTO nanostructures may also enhance the piezoelectric response and meanwhile facilitate ferroelectric switching.

4. CONCLUSIONS

In summary, self-assembled stripe [101]PTO nanostructures are fabricated on SRO-buffered STO(101) substrates by PLD. Diffraction contrast analysis and atomically resolved HAADF-STEM imaging reveal that the continuous polarization rotation forms from the left side to the right side in a [101]PTO nanostructure, whose rotation angle is almost up to 90°. Collaborated with phase-field simulations, it is proposed that the mechanism of the continuous polarization rotation could be ascribed to the surface positive charge accumulation due to the formation of oxygen vacancies at the surface of the [101]PTO layer. PFM measurements demonstrate that the continuous polarization rotation configuration and the formation of stripe nanostructures can convey superior piezoelectric responses in [101]PTO nanostructures. This work provides us a new approach to modulate the multiple polarization states and improve the piezoelectric responses of ferroelectrics.

■ ASSOCIATED CONTENT

Supporting Information

The Supporting Information is available free of charge on the ACS Publications website at DOI: 10.1021/acs.jpcc.9b04654.

High-resolution HAADF-STEM imaging and the polarization vector map of [001]PTO thin film; three-dimension schematic of a [101]PTO nanostructure; and details of phase-field simulations (PDF)

■ AUTHOR INFORMATION

Corresponding Authors

*E-mail: ylzhu@imr.ac.cn (Y.Z.).
*E-mail: xlma@imr.ac.cn (X.M.).

ORCID

Yinlian Zhu: 0000-0002-0356-3306

Author Contributions

Y.L.Z. and X.L.M. conceived the project of interfacial characterization in oxides by using aberration-corrected STEM. Y.P.F., Y.L.Z., and X.L.M. designed the experiments. Y.P.F. performed the thin-film growth and STEM observations. H.Z. and Y.J.W. carried out Phase-field simulations. Y.L.T., M.J.Z., M.J.H., W.R.G., and J.Y.M. participated in the thin-film growth and STEM imaging. All authors contributed to the discussions and manuscript preparation.

Notes

The authors declare no competing financial interest.

■ ACKNOWLEDGMENTS

This work is supported by the Key Research Program of Frontier Sciences CAS (QYZDJ-SSW-JSC010), the National Natural Science Foundation of China (nos. 51671194, 51571197), and National Basic Research Program of China (2014CB921002), Y. L. T. acknowledges the IMR SYNL-T.S. Kê Research Fellowship and the Youth Innovation Promotion Association CAS (no. 2016177). We are grateful to B. Wu and L.X. Yang of this lab for their technical support on the Titan platform of G2 60−300 kV aberration-corrected scanning transmission electron microscope.

■ REFERENCES

(1) Scott, J. F. Applications of Modern Ferroelectrics. *Science* **2007**, *315*, 954−959.
(2) Martin, L. W.; Rappe, A. M. Thin-Film Ferroelectric Materials and Their Applications. *Nat. Rev. Mater.* **2017**, *2*, 16087.
(3) Tang, Y. L.; Zhu, Y. L.; Ma, X. L.; Borisevich, A. Y.; Morozovska, A. N.; Eliseev, E. A.; Wang, W. Y.; Wang, Y. J.; Xu, Y. B.; Zhang, Z. D.; et al. Observation of A Periodic Array of Flux-Closure Quadrants in Strained Ferroelectric $PbTiO_3$ Films. *Science* **2015**, *348*, 547−551.
(4) Yadav, A. K.; Nelson, C. T.; Hsu, S. L.; Hong, Z.; Clarkson, J. D.; Schlepütz, C. M.; Damodaran, A. R.; Shafer, P.; Arenholz, E.; Dedon, L. R.; et al. Observation of Polar Vortices in Oxide Superlattices. *Nature* **2016**, *530*, 198−201.
(5) Lu, L.; Nahas, Y.; Liu, M.; Du, H.; Jiang, Z.; Ren, S.; Wang, D.; Jin, L.; Prokhorenko, S.; Jia, C. L.; et al. Topological Defects with Distinct Dipole Configurations in $PbTiO_3/SrTiO_3$ Multilayer Films. *Phys. Rev. Lett.* **2018**, *120*, 177601.
(6) Li, L. Z.; Cheng, X. X.; Jokisaari, J. R.; Gao, P.; Britson, J.; Adamo, C.; Heikes, C.; Schlom, D. G.; Chen, L. Q.; Pan, X. Q. Defect-Induced Hedgehog Polarization States in Multiferroics. *Phys. Rev. Lett.* **2018**, *120*, 137602.
(7) Fu, H.; Cohen, R. E. Polarization Rotation Mechanism for Ultrahigh Electromechanical Response in Single-Crystal Piezoelectrics. *Nature* **2000**, *403*, 281−283.
(8) Ahart, M.; Somayazulu, M.; Cohen, R. E.; Ganesh, P.; Dera, P.; Mao, H.-k.; Hemley, R. J.; Ren, Y.; Liermann, P.; Wu, Z. Origin of Morphotropic Phase Boundaries in Ferroelectrics. *Nature* **2008**, *451*, 545−548.
(9) Gao, J.; Hu, X.; Liu, Y.; Wang, Y.; Ke, X.; Wang, D.; Zhong, L.; Ren, X. Ferroelectric Domain Walls Approaching Morphotropic Phase Boundary. *J. Phys. Chem. C* **2017**, *121*, 2243−2250.
(10) Catalan, G.; Janssens, A.; Rispens, G.; Csiszar, S.; Seeck, O.; Rijnders, G.; Blank, D. H.; Noheda, B. Polar Domains in Lead Titanate Films under Tensile Strain. *Phys. Rev. Lett.* **2006**, *96*, 127602.
(11) Catalan, G.; Lubk, A.; Vlooswijk, A. H. G.; Snoeck, E.; Magen, C.; Janssens, A.; Rispens, G.; Rijnders, G.; Blank, D. H. A.; Noheda, B. Flexoelectric Rotation of Polarization in Ferroelectric Thin Films. *Nat. Mater.* **2011**, *10*, 963−967.
(12) Zhang, S.; Guo, X.; Tang, Y.; Ma, D.; Zhu, Y.; Wang, Y.; Li, S.; Han, M.; Chen, D.; Ma, J.; et al. Polarization Rotation in Ultrathin Ferroelectrics Tailored by Interfacial Oxygen Octahedral Coupling. *ACS Nano* **2018**, *12*, 3681−3688.
(13) Feng, Y.; Tang, Y.; Ma, D.; Zhu, Y.; Zou, M.; Han, M.; Ma, J.; Ma, X. Thickness-Dependent Evolution of Piezoresponses and Stripe 90° Domains in (101)-Oriented Ferroelectric $PbTiO_3$ Thin Films. *ACS Appl. Mater. Interfaces* **2018**, *10*, 24627−24637.
(14) Zou, M. J.; Tang, Y. L.; Zhu, Y. L.; Feng, Y. P.; Wang, Y. J.; Han, M. J.; Zhang, N. B.; Ma, J. Y.; Wu, B.; Ma, X. L. Anisotropic Strain: A Critical Role in Domain Evolution in (111)- Oriented Ferroelectric Films. *Acta Mater.* **2019**, *166*, 503−511.
(15) Xu, R. J.; Karthik, J.; Damodaran, A. R.; Martin, L. W. Stationary Domain Wall Contribution to Enhanced Ferroelectric Susceptibility. *Nat. Commun.* **2014**, *5*, 3120.

DOI: 10.1021/acs.jpcc.9b04654
J. Phys. Chem. C 2019, 123, 19602−19609

(16) Xu, R.; Liu, S.; Grinberg, I.; Karthik, J.; Damodaran, A. R.; Rappe, A. M.; Martin, L. W. Ferroelectric Polarization Reversal via Successive Ferroelastic Transitions. *Nat. Mater.* **2015**, *14*, 79−86.
(17) Mtebwa, M.; Tagantsev, A. K.; Yamada, T.; Gemeiner, P.; Dkhil, B.; Setter, N. Single-Domain (110) $PbTiO_3$ Thin Films: Thermodynamic Theory and Experiments. *Phy. Rev. B* **2016**, *93*, 144113.
(18) Hutter, J. L.; Bechhoefer, J. Calibration of Atomic Force Microscope Tips. *Rev. Sci. Instrum.* **1993**, *64*, 1868−1873.
(19) Sader, J. E.; Chon, J. W. M.; Mulvaney, P. Calibration of Rectangular Atomic Force Microscope Cantilevers. *Rev. Sci. Instrum.* **1999**, *70*, 3967−3969.
(20) Li, Y. L.; Hu, S. Y.; Liu, Z. K.; Chen, L. Q. Effect of Substrate Constraint on the Stability and Evolution of Ferroelectric Domain Structures in Thin Films. *Acta Mater.* **2002**, *50*, 395−411.
(21) Glazer, A. M.; Mabud, S. A. Powder Profile Refinement of Lead Zirconate Titanate at Several Temperatures. II. Pure $PbTiO_3$. *Acta Crystallogr., Sect. B: Struct. Sci., Cryst. Eng. Mater.* **1978**, *34*, 1065−1070.
(22) Tang, Y. L.; Zhu, Y. L.; Meng, H.; Zhang, Y. Q.; Ma, X. L. Misfit Dislocations of Anisotropic Magnetoresistant $Nd_{0.45}Sr_{0.55}MnO_3$ Thin Films Grown on $SrTiO_3$(110) Substrates. *Acta Mater.* **2012**, *60*, 5975−5983.
(23) Pennycook, S. J.; Jesson, D. E. High-Resolution Z-Contrast Imaging of Crystals. *Ultramicroscopy* **1991**, *37*, 14−38.
(24) Tang, Y. L.; Zhu, Y. L.; Ma, X. L. On the Benefit of Aberration-Corrected HAADF-STEM for Strain Determination and Its Application to Tailoring Ferroelectric Domain Patterns. *Ultramicroscopy* **2016**, *160*, 57−63.
(25) Mtebwa, M.; Mazzalai, A.; Sandu, C. S.; Crassous, A.; Setter, N. Engineered *a/c* Domain Patterns in Multilayer (110) Epitaxial $Pb(Zr,Ti)O_3$ Thin Films: Impact on Domain Compliance and Piezoelectric Properties. *AIP Adv.* **2016**, *6*, 055104.
(26) Jesson, D. E.; Chen, K. M.; Pennycook, S. J. Kinetic Pathways to Strain Relaxation in the Si-Ge System. *MRS Bull.* **1996**, *21*, 31−37.
(27) Nonomura, H.; Fujisawa, H.; Shimizu, M.; Niu, H.; Honda, K. Self-Assembled $PbTiO_3$ Nano-Islands Prepared on $SrTiO_3$ by Metalorganic Chemical Vapor Deposition. *Jpn. J. Appl. Phys.* **2003**, *42*, 5918−5921.
(28) Eglitis, R. I.; Vanderbilt, D. *Ab initio* Calculations of $BaTiO_3$ and $PbTiO_3$ (001) and (011) Surface Structures. *Phys. Rev. B: Condens. Matter Mater. Phys.* **2007**, *76*, 155439.
(29) Zubko, P.; Catalan, G.; Tagantsev, A. K. Flexoelectric Effect in Solids. *Annu. Rev. Mater. Res.* **2013**, *43*, 387−421.
(30) Zubko, P.; Catalan, G.; Buckley, A.; Welche, P. R.; Scott, J. F. Strain-Gradient-Induced Polarization in $SrTiO_3$ Single Crystals. *Phys. Rev. Lett.* **2008**, *99*, 167601.
(31) Lee, D.; Yoon, A.; Jang, S. Y.; Yoon, J. G.; Chung, J. S.; Kim, M.; Scott, J. F.; Noh, T. W. Giant Flexoelectric Effect in Ferroelectric Epitaxial Thin Films. *Phys. Rev. Lett.* **2011**, *107*, 057602.
(32) Li, Z.; Wang, Y.; Tian, G.; Li, P.; Zhao, L.; Zhang, F.; Yao, J.; Fan, H.; Song, X.; Chen, D.; et al. High-Density Array of Ferroelectric Nanodots with Robust and Reversibly Switchable Topological Domain States. *Sci. Adv.* **2017**, *3*, No. e1700919.
(33) Han, M.-J.; Wang, Y.-J.; Tang, Y.-L.; Zhu, Y.-L.; Ma, J.-Y.; Geng, W.-R.; Zou, M.-J.; Feng, Y.-P.; Zhang, N.-B.; Ma, X.-L. Shape and Surface Charge Modulation of Topological Domains in Oxide Multiferroics. *J. Phys. Chem. C* **2019**, *123*, 2557−2564.
(34) Zhong, G.; An, F.; Bitla, Y.; Wang, J.; Zhong, X.; Yu, J.; Gao, W.; Zhang, Y.; Tan, C.; Ou, Y.; et al. Deterministic, Reversible, and Nonvolatile Low-Voltage Writing of Magnetic Domains in Epitaxial $BaTiO_3/Fe_3O_4$ Heterostructure. *ACS Nano* **2018**, *12*, 9558−9567.
(35) Rodriguez, B. J.; Callahan, C.; Kalinin, S. V.; Proksch, R. Dual-Frequency Resonance-Tracking Atomic Force Microscopy. *Nanotechnology* **2007**, *18*, 475504.
(36) Peng, J. J.; Song, C.; Cui, B.; Li, F.; Mao, H. J.; Wang, G. Y.; Pan, F. Manipulation of Orbital Occupancy by Ferroelectric Polarization in $LaNiO_3/BaTiO_{3-\delta}$ Heterostructures. *Appl. Phys. Lett.* **2015**, *107*, 182904.
(37) Li, W.; Wang, Y.; Nie, P.; Hu, Q.; Yang, Y.; Yuan, G. Enhanced Switching Characteristics and Piezoelectric Response in Epitaxial $BiFeO_3$−$TbMnO_3$ Thin Films. *Phys. B* **2015**, *466*−*467*, 11−15.
(38) Sun, W.; Yu, Q.; Li, J.; Li, J.-F. Shifted Morphotropic Phase Boundary in [111]-Oriented Nb-Doped $Pb(Zr_xTi_{1-x})O_3$ Epitaxial Films: Insights into Piezoelectricity and Domain Variation. *J. Phys. Chem. C* **2015**, *119*, 19891−19896.
(39) Lee, H.-Y.; Luo, J.; Zhou, Z.; Sun, W.; Li, J.-F. Macroscopic and Local Approaches of Phase Transition in Sol-Gel Synthesized $(Bi_{0.5}Na_{0.5})TiO_3$-$SrTiO_3$ Thin Films. *Phys. Chem. Chem. Phys.* **2018**, *20*, 15236−15243.
(40) Pertsev, N. A.; Emelyanov, A. Y. Domain−Wall Contribution to the Piezoelectric Response of Epitaxial Ferroelectric Thin Films. *Appl. Phys. Lett.* **1997**, *71*, 3646−3648.
(41) Nahas, Y.; Akbarzadeh, A.; Prokhorenko, S.; Prosandeev, S.; Walter, R.; Kornev, I.; Iniguez, J.; Bellaiche, L. Microscopic Origins of the Large Piezoelectricity of Lead Free $(Ba,Ca)(Zr,Ti)O_3$. *Nat. Commun.* **2017**, *8*, 15944.
(42) Nagarajan, V.; Roytburd, A.; Stanishevsky, A.; Prasertchoung, S.; Zhao, T.; Chen, L.; Melngailis, J.; Auciello, O.; Ramesh, R. Dynamics of Ferroelastic Domains in Ferroelectric Thin Films. *Nat. Mater.* **2003**, *2*, 43−47.

DOI: 10.1021/acs.jpcc.9b04654
J. Phys. Chem. C 2019, 123, 19602−19609